Composite Structures 237 (2020) 111868

Contents lists available at ScienceDirect

Composite Structures

journal homepage: www.elsevier.com/locate/compstruct

Energy absorption capability of composite bolted joints undergoing extended bearing failure

Jazib Hassan[a], Thomas Feser[b], Ronan M. O'Higgins[a], Matthias Waimer[b], Conor T. McCarthy[a], Nathalie Toso[b], Michael E. Byrne[a,b], Michael A. McCarthy[a,*]

[a] Irish Composites Centre (ICOMP), Bernal Institute, School of Engineering, University of Limerick, Ireland
[b] German Aerospace Center (DLR), Institute of Structures and Design, Stuttgart, Germany

ARTICLE INFO

Keywords:
Composite bolted joints
Mechanical testing
Energy absorption
Bearing failure

ABSTRACT

Innovative crashworthiness strategies are needed for future narrow-body composite fuselage aircraft due to limited crash energy absorption capability below the cargo floor. A recently-proposed approach is to use specially-designed "tension absorber" joints which absorb energy through an extended bearing failure process. To explore the design space, experimental tests are performed on pin-loaded joints in a widely-used carbon fibre/epoxy composite, with varying stacking sequence, pin diameter and laminate thickness. A bespoke rig is used to pull the pin completely through the laminate. Performance parameters include ultimate bearing strength, mean crushing stress and mass-specific energy absorption. Three-dimensional computed tomography (3D CT) and scanning electron microscopy are used to examine failure and damage. Diameter-to-thickness ratio is found to be an excellent predictor of energy absorption, with small values giving best results, provided the thickness is sufficient to avoid global bending of the specimen. The use of a well-characterised material and availability of 3D CT data enables the results to be used for validation of analysis tools.

1. Introduction

The use of carbon fibre reinforced polymer (CFRP) composites in wide-body commercial aircraft fuselages is now established practice, as witnessed by the Airbus A350 XWB and the Boeing 787 Dreamliner. To achieve certification, an equivalent level of occupant safety to that of previously certified, wide-body, metallic fuselage transports had to be demonstrated in a "foreseeable survivable impact event", defined as a 30 ft/s (9.14 m/s) vertical drop test [1,2]. Due to the relatively large height of the space below the cargo floor in wide-body aircraft, it was possible to achieve the bulk of the energy absorption requirements via a sub-cargo structure involving crushable composite beams [3]. However, in single-aisle (i.e. narrow-body) aircraft, the height of the sub-cargo area is much less, so additional energy absorbing structures or devices will be required [4].

To address this issue, Airbus and DLR have been working on new single-aisle composite fuselage concepts, one of which involves the use of "tension absorbing" composite joints [4–7]. Most energy-absorption solutions are developed for compressive loads. However, tensile-loaded absorbers also exist, e.g. in fall-arrest devices for industrial workers [8]. The proposed Airbus/DLR concepts involve modification of joints in areas known to be loaded in tension during a crash landing, to enable them to absorb considerable amounts of energy. As illustrated in Fig. 1, the targeted areas are the cargo and passenger cross-beams, which are loaded in tension as the fuselage deforms into a more oval shape during a vertical impact. It has been predicted, via full-scale simulations, that more than 50% of the overall absorbed energy could be taken by such tension absorbers, so that much less energy would need to be absorbed by the sub-cargo crush zone [4]. This has the added benefit of allowing a lighter cargo cross-beam.

Failure of composite bolted joints is considerably more complex than that of metallic joints and has been extensively studied in the past [9,10]. Composite aircraft joints are typically designed to fail in bearing rather than in catastrophic failure modes such as net tension or shear out. In bearing failure, the bolts crush the material in front of the hole, thereby absorbing some energy, and the parts remain connected. In a severe overloading, such as a crash, the energy absorbed by standard joints is limited because the crushing process is generally interrupted by bolts pulling through the holes in the through-thickness direction ("pull-through" failure). For countersunk fasteners, this can be preceded by partial or complete shear-off of the bolt heads [11].

In tension-absorbing joints, the aim is to continue the crushing

* Corresponding author.
E-mail address: michael.mccarthy@ul.ie (M.A. McCarthy).

https://doi.org/10.1016/j.compstruct.2020.111868
Received 25 October 2019; Received in revised form 3 December 2019; Accepted 2 January 2020
Available online 18 January 2020

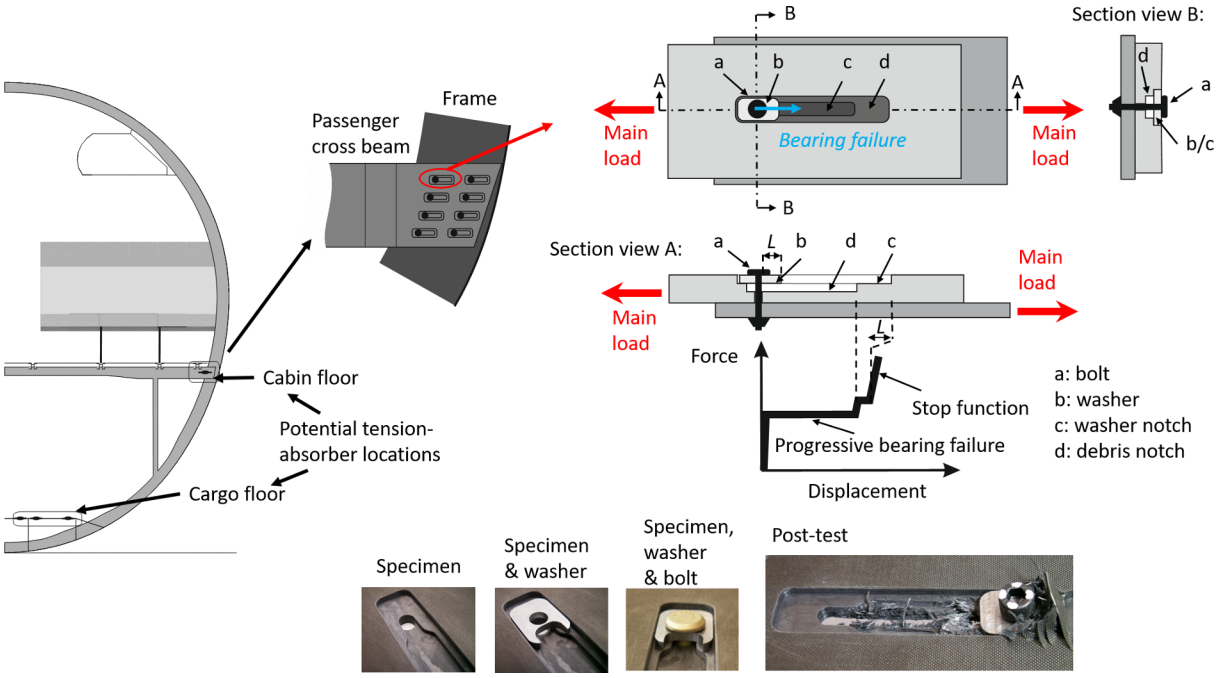

Fig. 1. Tension-absorbing joint concept for narrow-body composite fuselage [4,7].

process over much longer distances (referred to here as "extended bearing failure"), thereby enabling significant levels of energy absorption. As illustrated in Fig. 1, this is achieved via specially-designed washers, and slots cut into the composite, which guide the bolt's travel and prevent it from fracturing or pulling through. The flow of debris is also controlled so as not to impede bolt progress. Examples of various designs can be found in [4,7]. The concept was originally proposed for overhead luggage racks [12] and energy absorbing seats in helicopters [13].

To explore the design space for such tension absorbers, Airbus and DLR have undertaken experimental and numerical studies on single and multi-bolt coupons and structural elements [4–7,14]. They have also studied a simplified version of the problem, namely a pin being pulled through a composite plate, to examine the effects of individual material and geometric parameters, since the influence of debris in the actual joints is unpredictable and can mask the effects of other variables. Bergmann [15], Heimbs and Bergmann [16] and Bergmann et al. [17] have used the pin-loaded setup to examine the energy-absorbing performance of a wide variety of fibre and matrix materials, as well as fibre architectures and layups. They also performed material characterisation of woven fabric HTA/RTM6 and carried out pin bearing simulations using a layered shell approach. Feser and Waimer [14] developed a stacked shell approach with cohesive elements to model delamination, and applied it to the experiments in [4–7]. The developed methods worked well, but full validation against experiments was hampered by the unavailability of complete material data for the material used.

In an EU-funded project, DLR and the University of Limerick are collaborating to extend the studies on tension absorbers in [4–7,14–18]. In the present work, the approach in [15–17] is followed, whereby a pin is pulled through a laminate to study the effects of geometric and material parameters on bearing strength and energy absorption capability. Bearing strength is relevant because tension-absorbing joints must also function appropriately during in-service loads. Fifteen configurations are tested, involving variations in pin diameter, laminate thickness and stacking sequence. The chosen material is IM7/8552 carbon/epoxy, which has been used in the third world-wide composites failure exercise [19]. All the parameters needed to calibrate damage and failure models for this material have been extensively characterised already [20–23], so the results herein can be used for validation of models without further material tests. The test campaign is split between two laboratories (DLR and ULIM), to examine machine-specific influences, if any. Tests are performed at quasi-static rates (dynamic tests are planned for later), and three-dimensional computed tomography (3D CT) and scanning electron microscopy (SEM) are used to investigate failure mechanisms.

2. Materials and methods

2.1. Specimen and test campaign details

HexPly® IM7/8552 (EU version: 134 gsm) carbon fibre/epoxy composite was obtained in pre-preg form with a nominal ply thickness of 0.125 mm. Quasi-isotropic panels were laid up by hand and consolidated in the ULIM autoclave according to manufacturer specifications. Specimens with the geometry shown in Fig. 2 were extracted via water jet cutting. The geometry was selected following a prior study [24], considering the grip systems of the two test machines and a desire to avoid specimen damage reaching all the way to the edge. Holes were drilled using solid carbide tooling with an H7 tolerance.

As outlined in Table 1, fifteen configurations were tested, with variable stacking sequence, pin diameter and laminate thickness. Using the nomenclature in [25,26], the 2 mm and 3 mm thick stacking

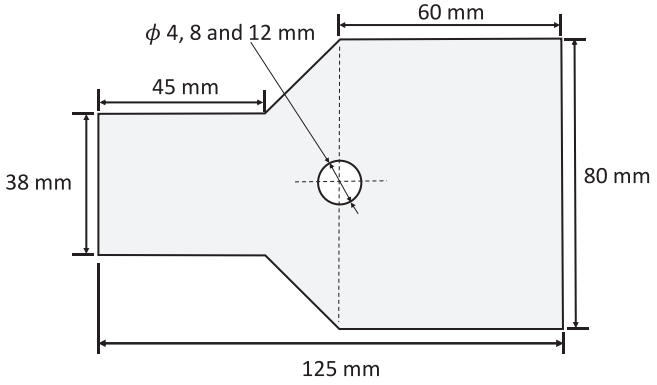

Fig. 2. Specimen geometry.

Table 1
Test parameters (nominal ply thickness = 0.125 mm). Four repeats performed of each case. For the 10 boldfaced configurations, an additional interrupted test was performed and examined with microscopy.

Configuration	Code	Stacking sequence	Bolt diameter (mm)	Thickness (mm)
1	D4_T1	$[45/-45/90/0]_s$	4	1
2	D8_T1	$[45/-45/90/0]_s$	8	1
3	D12_T1	$[45/-45/90/0]_s$	12	1
4	**DS_D4_T2**	$[45/-45/90/0]_{2s}$	**4**	**2**
5	**DS_D8_T2**	$[45/-45/90/0]_{2s}$	**8**	**2**
6	**DS_D12_T2**	$[45/-45/90/0]_{2s}$	**12**	**2**
7	DS_D4_T3	$[45/-45/90/0]_{3s}$	4	3
8	**DS_D8_T3**	$[45/-45/90/0]_{3s}$	**8**	**3**
9	**DS_D12_T3**	$[45/-45/90/0]_{3s}$	**12**	**3**
10	**BK_D4_T2**	$[45_2/-45_2/90_2/0_2]_s$	**4**	**2**
11	**BK_D8_T2**	$[45_2/-45_2/90_2/0_2]_s$	**8**	**2**
12	**BK_D12_T2**	$[45_2/-45_2/90_2/0_2]_s$	**12**	**2**
13	BK_D4_T3	$[45_3/-45_3/90_3/0_3]_s$	4	3
14	**BK_D8_T3**	$[45_3/-45_3/90_3/0_3]_s$	**8**	**3**
15	**BK_D12_T3**	$[45_3/-45_3/90_3/0_3]_s$	**12**	**3**

sequences are labelled “dispersed” or “blocked” depending on whether the stacking sequence is $[45/-45/90/0]_{ns}$ with $n = 2$, 3 or $[45_m/-45_m/90_m/0_m]_s$ with $m = 2$, 3, respectively. A code is used to identify the stacking sequence, pin diameter and laminate thickness (e.g. DS_D4_T2 or BK_D12_T3). For the 1 mm thick specimens DS/BK is omitted, since the 1 mm thick $[45/-45/90/0]_s$ laminate could be considered the “root” stacking sequence of the dispersed test series (with $n = 1$), or the blocked test series (with $m = 1$). Thus, there are five stacking sequences in total. Four repeats of each configuration were performed, two each at ULIM and DLR, giving 60 tests in all, with 10 further interrupted tests undertaken for CT and SEM analysis (the boldfaced configurations in Table 1).

2.2. Experimental set-up

Servo-hydraulic test machines were used, a Zwick 100 kN machine at ULIM, and an Instron VHS100/20M machine at DLR. Hydraulic grips were used at ULIM, while mechanical grips were used at DLR. The bespoke test rig, shown in Fig. 3(a), was designed to be low mass since it will also be used in dynamic tests. It contains three main components: a hardened steel pin, a pair of steel tensions rods used to load the pin, and a steel pulling plate bolted to the tension rods. As shown in Fig. 3(b), the steel plate was gripped at the loading end of the servo-hydraulic machine, and the composite specimen was gripped at the fixed end. By using different thickness steel plates for the different thickness composite specimens, and carefully centring the specimen between the tension rods, sufficient space was provided for debris outflow (2.5 mm on each side). A test velocity of 10 mm/min was chosen. Portement et al. [27] showed for a similar pin-crushing problem that strain rates up to 60 mm/min cause no noticeable strain rate effects, so the velocity used here can be regarded as quasi-static. Specimens had one surface prepared for DIC analysis, but as shown in Fig. 3(c), surface plies partially peeled off as soon as crushing began so the DIC data revealed little and is not presented here. Identifiable black dots were marked on the pin surface for measurement of pin displacement using DIC software (DaVis, a product of LaVision GmbH, at ULIM and GOM Correlate, a product of GOM GmbH, at DLR).

3. Results and discussion

3.1. Sample load-deflection curves and performance parameter definitions

Fig. 4(a) shows complete load-displacement curves for four repeats (two from each laboratory) of one configuration, while Fig. 4(b) shows the response over the first 5 mm. Good repeatability is observed and, in general, no statistically significant difference was found between the results from DLR and ULIM. Three main phases can be identified in the load-displacement response:

Phase 1: Linearly increasing load, with slight non-linearity just prior to attainment of maximum load, F_{max}.
Phase 2: Sharp load drop indicating “ultimate bearing failure”, followed by establishment of a stable crushing load, which rises slightly until about 5 mm, and then stays fairly constant until 40 mm. Based on this, mean crushing force, F_{mean}, is defined as the average force between 5 mm and 40 mm displacement.
Phase 3: Final failure as the bolt pulls through the end of the laminate, during which the load in some cases shows a small increase before dropping off to zero.

Fig. 5 shows an example of how the test series parameters affect the response. Results are for 2 mm thick, blocked stacking sequence specimens tested with three different diameter pins. As expected, increasing pin diameter leads to higher values of F_{max} and F_{mean}, which can be partially attributed to an increasing volume of crushed material.

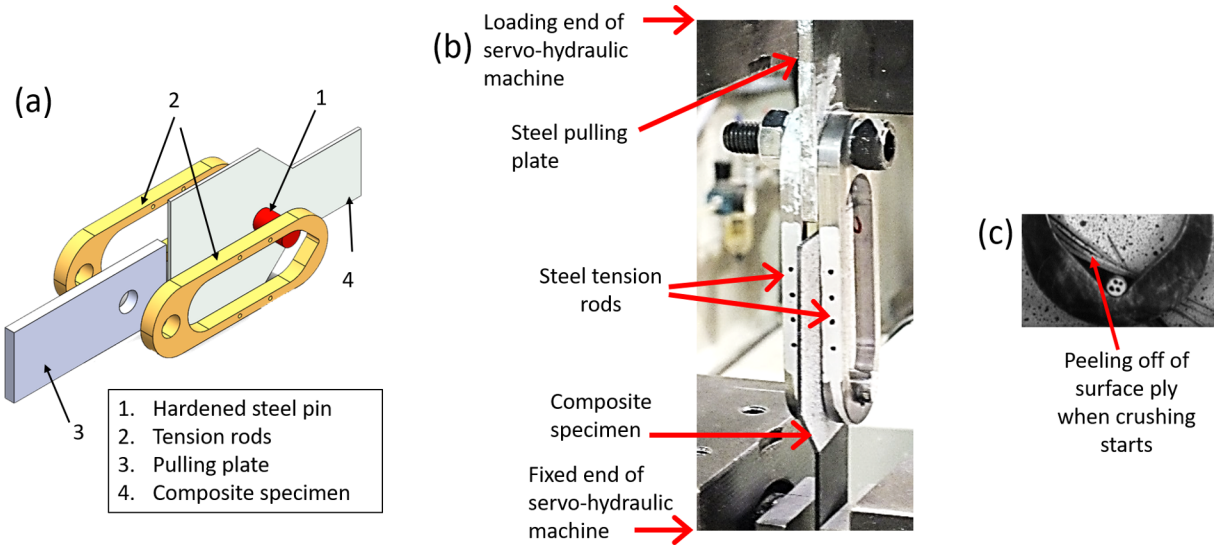

Fig. 3. (a) Exploded view of test rig, (b) side view of test setup, (c) surface ply behaviour.

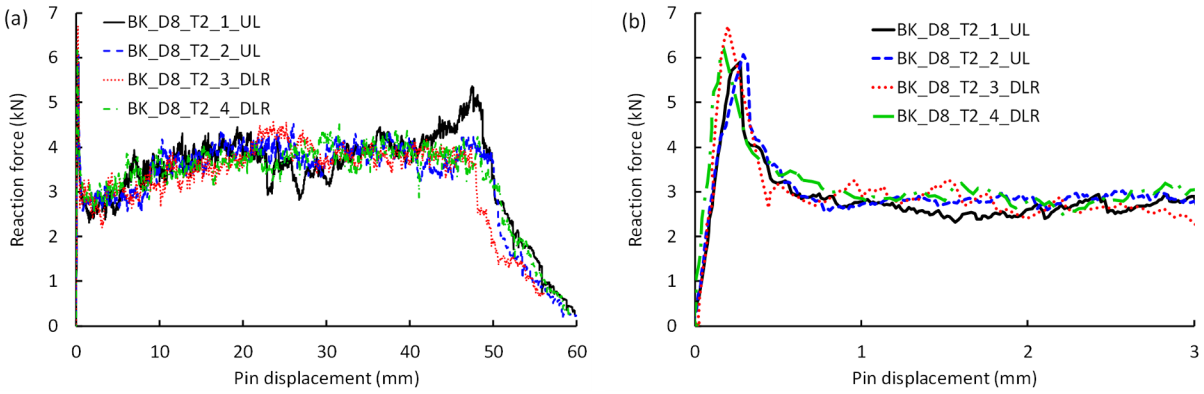

Fig. 4. (a) Force-displacement response of BK_D8_T2 specimens, i.e. 2 mm thick with blocked $[45_2/-45_2/90_2/0_2]_s$ stacking sequence, tested with 8 mm diameter pin. (b) Response over first 5 mm.

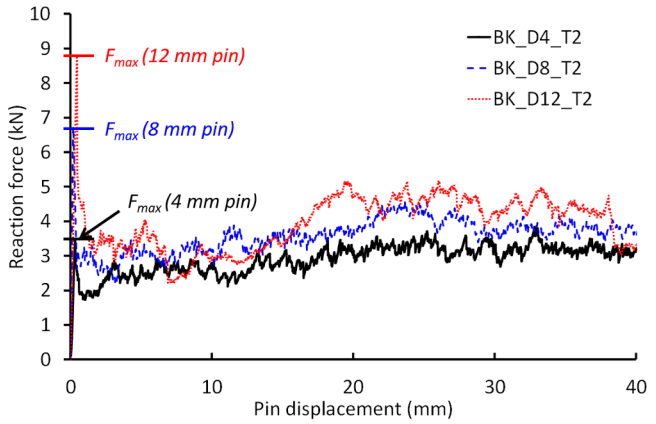

Fig. 5. Effect of pin diameter for a 2 mm thick, blocked $[45_2/-45_2/90_2/0_2]_s$ laminate.

However, the ratio F_{mean}/F_{max} is different for each diameter, illustrating that the ultimate bearing force does not necessarily scale with diameter at the same rate as the mean crushing force.

To allow comparisons on a material level, the following performance parameters are defined. The ultimate bearing strength (UBS), σ_{ult} is based on the maximum load achieved and defined in accordance with D 5961/D 5961M [28]:

$$\sigma_{ult} = \frac{F_{\max}}{D \cdot t} \tag{1}$$

where D is the pin diameter and t is laminate thickness. The mean crushing stress (MCS) is:

$$\sigma_{mean} = \frac{F_{mean}}{D \cdot t} \tag{2}$$

where, as noted above, F_{mean} is calculated between 5 mm and 40 mm displacement. The mass-specific energy absorption (SEA) is a measure used to characterise materials and structures such as crushable beams and tubes. It is defined as the integral of the force-deflection curve divided by the mass of destroyed material. To allow comparison with such studies, for the current pin-crushing problem, it has been estimated in [16] that, for materials with brittle fibres, the width of destroyed material is 20% larger than the pin diameter. For comparison with that study, the same figure is used here, although as will be seen, it is not easy to define an exact value, as damage spreads to a different extent in each ply. In any case, values can be scaled, if desired, by changing the value of 1.2 in the equation below:

$$SEA = \frac{1}{m_{absorbed}} \int_0^{s_m} F \cdot ds = \frac{1}{1.2\rho t D s_m} \int_0^{s_m} F \cdot ds \tag{3}$$

where ρ is material density and s_m is maximum pin displacement, which is taken here as 40 mm for all tests.

3.2. Performance parameter results

Fig. 6 summarises all the test findings on the variation of UBS, MCS and SEA with laminate thickness, pin diameter, and stacking sequence. Dispersed laminate results are on the left (Fig. 6(a), (c) and (e)), while blocked laminate results are on the right (Fig. 6(b), (d) and (f)). The 1 mm thick specimens are included in both the dispersed and blocked graphs since, as explained in Section 2.1, they could be considered to be the root stacking sequence for the dispersed test series (with $n = 1$) or the blocked test series (with $m = 1$). Note that UBS, MCS and SEA all involve normalisation of the force by $D \cdot t$ (Eqs. (1)–(3)), so a change in any of these quantities with D or t indicates the relevant force (e.g. $F_{\max}$ for UBS, F_{mean} for MCS etc.) does not scale proportionally with D or t.

The UBS values, Fig. 6(a) and (b), range between 298 and 621 MPa, which is similar to the range of previously reported values for this material with a quasi-isotropic layup [29]. The largest bearing strength is for the smallest pin with the thickest, dispersed laminate (DS_D4_T3), and is more than double that of the D12_T1 configuration. The variation in SEA is also very substantial. The SEA for the BK_D4_T3 configuration is 189 kJ/kg, which is almost three times the SEA of the D12_T1 configuration (66 kJ/kg). Clearly the choice of pin diameter and laminate thickness are important considerations in the design of tension-absorbing joints.

Addressing the effect of pin diameter in detail, the following observations can be made (with supporting detail provided below each observation):

(i) *UBS (Fig. 6(a) and (b)) decreases with increasing pin diameter and the effect is somewhat more definitive for blocked laminates. D4_T1 is an outlier since its UBS is less than that for D8_T1.*

Detail: For 2 mm thick, dispersed laminates, the UBS for 8 mm and 12 mm pins is 5% and 12% less respectively than for 4 mm pins. The corresponding reductions for a 3 mm thick, dispersed laminate are 8% and 20%. For a 2 mm thick, blocked laminate, the figures are 17% and 22%, and for a 3 mm thick blocked laminate the figures are also 17% and 22%.

(ii) *MCS (Fig. 6(c) and (d)) decreases substantially with increasing pin diameter for all thicknesses and stacking sequences. The effect is more pronounced for blocked laminates than for dispersed laminates.*

Detail: For 1 mm thick laminates, the MCS for 8 mm and 12 mm pins is 25% and 44% less respectively than the value for a 4 mm pin. The corresponding reductions for a 2 mm thick, dispersed laminate are 13%

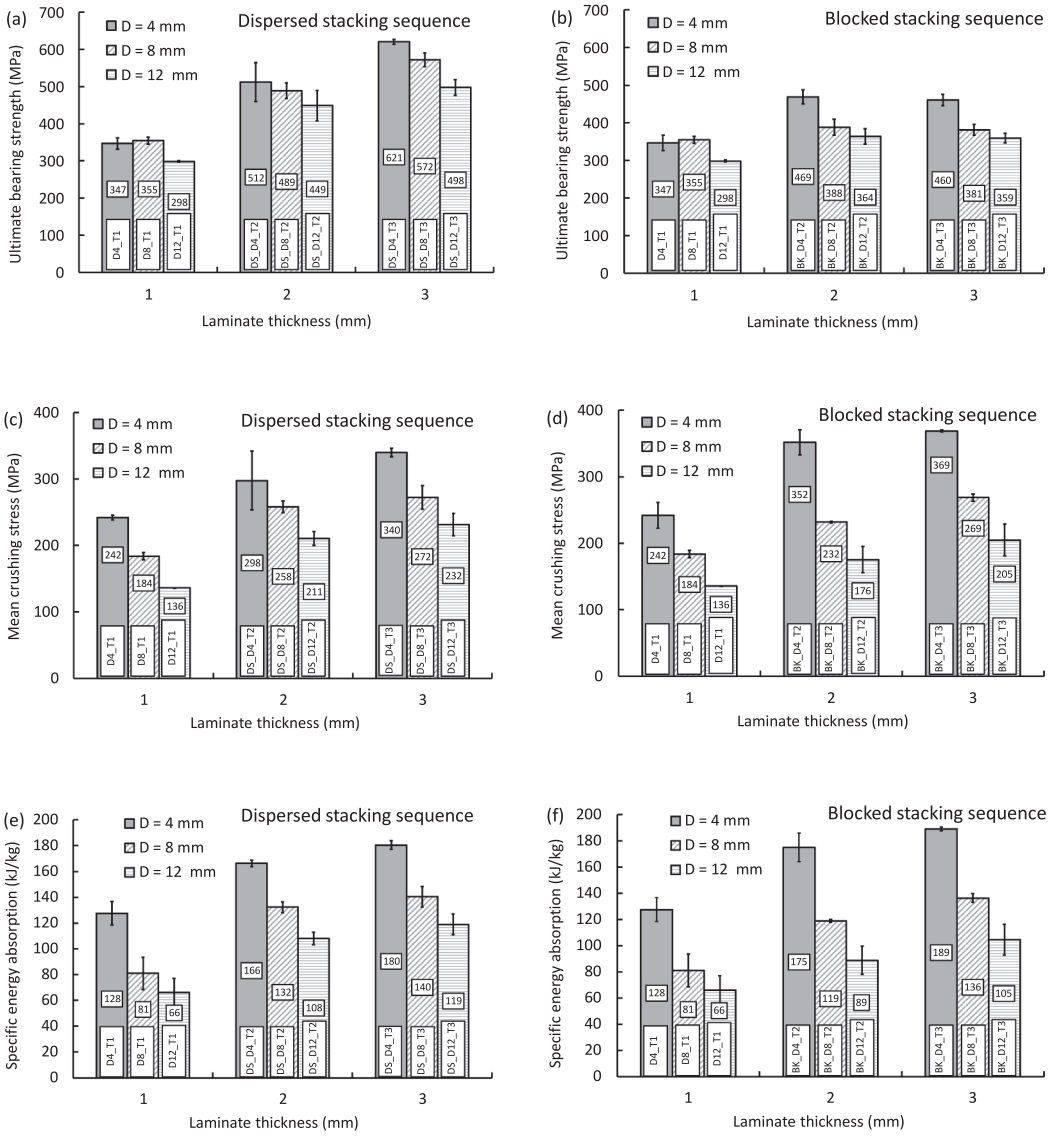

Fig. 6. Summary results for all 60 tests, (a) UBS dispersed stacking sequence, (b) UBS blocked stacking sequence, (c) MCS dispersed stacking sequence, (d) MCS blocked stacking sequence, (e) SEA dispersed stacking sequence, (f) SEA blocked stacking sequence.

and 29%, and for a 3 mm, dispersed laminate are 20% and 32%. For a 2 mm thick, blocked laminate, the corresponding figures are 34% and 50%, and for a 3 mm blocked laminate 27% and 44%.

(iii) *SEA (Fig. 6(e) and (f)) decreases substantially with increasing pin diameter for all thicknesses and stacking sequences. Again the effect is most pronounced for blocked laminates.*

Detail: For a 1 mm thick laminate, the SEA for 8 mm and 12 mm pins is 37% and 48% less respectively than the value for a 4 mm pin. The corresponding reductions for a 2 mm thick, dispersed laminate are 20% and 35%, and for a 3 mm, dispersed laminate are 22% and 34%. For a 2 mm thick, blocked laminate, the corresponding figures are 32% and 49%, and for a 3 mm blocked laminate 28% and 44%.

Summarising the effect of pin diameter, we have:

Main result 1: Increasing pin diameter leads to lower UBS, MCS and SEA, with the effect being more pronounced for blocked laminates. The one outlier is D4_T1 which has a lower UBS than D8_T1.

Turning to the effect of laminate thickness:

(iv) *UBS (Fig. 6(a) and (b)) increases as thickness increases from 1 to 2 mm. For a further increase to 3 mm, UBS increases for dispersed laminates (not as much as from 1 to 2 mm) but stays the same for blocked laminates.*

Detail: Taking the UBS of a 1 mm thick specimen as the baseline, dispersed laminates with a 4 mm pin show a 48% increase in UBS for a 2 mm thick laminate and a 79% increase for a 3 mm thick laminate (i.e. increasing from 2 to 3 mm adds an extra 31% to UBS). The corresponding increases for an 8 mm pin are 38% and 61%, and for a 12 mm pin are 51% and 67%. For blocked laminates, as the thickness changes from 1 mm to 2 mm, the UBS increases by 35%, 9% and 22% for 4 mm, 8 mm and 12 mm pins respectively, while no statistically significant change occurs for a thickness change from 2 mm to 3 mm.

(v) *MCS (Fig. 6(c) and (d)) increases with increasing thickness. Similarly to UBS, the increase in MCS is larger as the thickness changes from 1 mm to 2 mm than when it changes from 2 mm to 3 mm, but unlike UBS, blocked laminates do exhibit an increase in MCS as thickness changes from 2 mm to 3 mm.*

Detail: Taking the MCS of a 1 mm thick specimen as baseline,

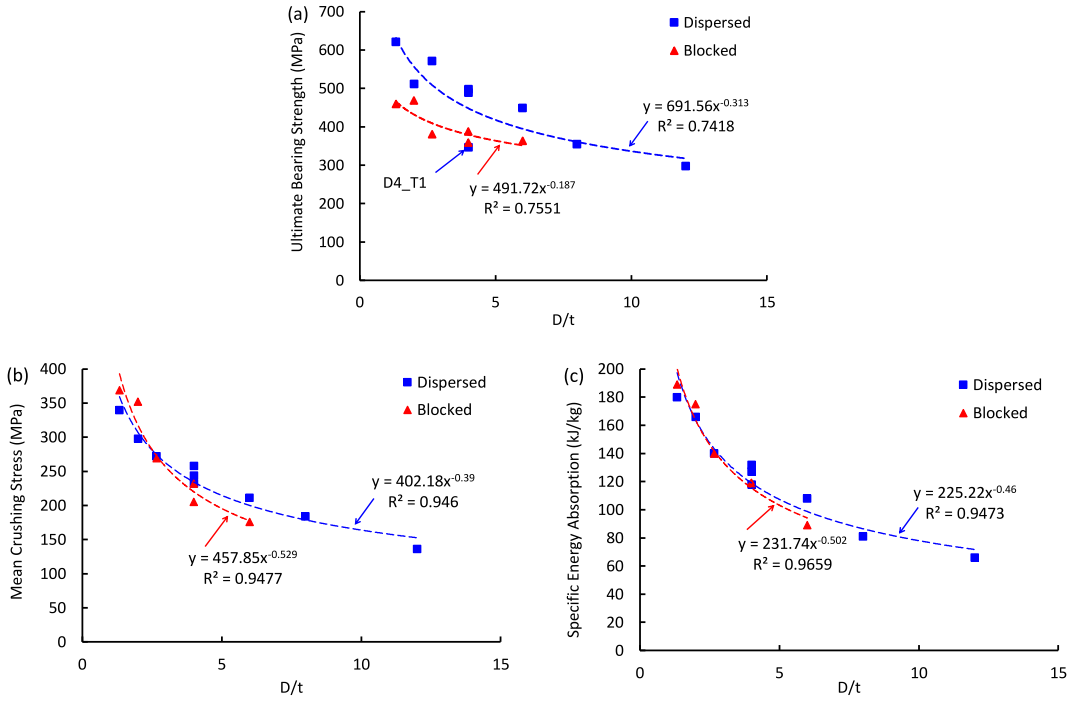

Fig. 7. Performance parameters plotted versus *D/t*, (a) ultimate bearing strength, (b) mean crushing stress (c) mass-specific energy absorption.

dispersed laminates with a 4 mm pin show a 22% increase in MCS for a 2 mm thickness and a 39% increase for a 3 mm thickness (i.e. increasing from 2 to 3 mm adds an extra 17% to MCS). The corresponding increases for an 8 mm pin are 40% and 48%, and for a 12 mm pin are 55% and 71%. For blocked laminates, again taking the 1 mm thick specimen as baseline, with a 4 mm pin, we find a 44% increase in MCS for a 2 mm thickness, and a 51% increase for a 3 mm thickness. The corresponding increases for an 8 mm pin are 26% and 46%, and for a 12 mm pin are 29% and 51%.

(vi) *SEA (Fig. 6(e) and (f)) shows large increases as thickness increases from 1 mm to 2 mm, and smaller increases as thickness increases further to 3 mm.*

Detail: Taking the SEA of a 1 mm thick specimen as baseline, dispersed laminates with a 4 mm pin show a 30% increase in MCS for a 2 mm thickness and a 41% increase for a 3 mm thickness (i.e. increasing from 2 to 3 mm adds an extra 11% to MCS). The corresponding increases for an 8 mm pin are 63% and 73%, and for a 12 mm pin are 64% and 80%. For blocked laminates, again taking the 1 mm thick specimen as baseline, with a 4 mm pin, we find a 37% increase in MCS for a 2 mm thickness, and a 48% increase for a 3 mm thickness. The corresponding increases for an 8 mm pin are 47% and 68%, and for a 12 mm pin are 35% and 59%.

Summarising the effect of thickness:

Main result 2: Increasing thickness from 1 mm to 2 mm leads to significant increases in UBS, MCS and SEA. A further increase to 3 mm results in smaller increases in all quantities except the UBS of blocked laminates, for which no change occurs.

Finally the effects of stacking sequence are as follows (the 1 mm laminates are ignored here):

(vii) *UBS (Fig. 6(a) and (b)) is higher for dispersed laminates than for blocked laminates. The effect is larger for thicker laminates.*

Detail: Comparing the value labels in Fig. 6(a) and (b), it can be seen that, for 2 mm thickness, the UBS values for the dispersed laminate are 9% higher (512 versus 469 MPa) for the 4 mm pin, 26% higher (489 versus 388 MPa) for the 8 mm pin, and 23% higher (449 versus 364 MPa) for the 12 mm pin. For the 3 mm thick specimens, the corresponding values are 35% (621 versus 460 MPa) for the 4 mm pin, 50% (572 versus 381 MPa) for the 8 mm pin, and 39% (498 versus 359 MPa) for the 12 mm pin.

(viii) *MCS (Fig. 6(c) and (d)) is highest for blocked laminates for 4 mm pins, and dispersed laminates for 8 mm and 12 mm pins.*

Detail: For a 4 mm pin, MCS is higher for blocked laminates by 18% for 2 mm thickness, and 9% for 3 mm thickness. For an 8 mm pin, it is slightly higher for the dispersed laminates (by 11% for 2 mm thickness and 1% for 3 mm thickness). For a 12 mm pin, it is higher for dispersed laminates (by 20% for 2 mm thickness and 13% for 3 mm thickness).

(ix) *SEA (Fig. 6(e) and (f)) is (like MCS) highest for blocked laminates for 4 mm pins, and dispersed laminates for 8 mm and 12 mm pins.*

Detail: For a 4 mm pin, SEA is higher for blocked laminates by 30% for 2 mm thickness, and 5% for 3 mm thickness. For an 8 mm pin, it is higher for dispersed laminates by 11% for 2 mm thickness and 3% for 3 mm thickness. For a 12 mm pin, it is higher for dispersed laminates by 21% for 2 mm thickness and 13% for 3 mm thickness.

Summarising the effect of stacking sequence:

Main result 3: Dispersed laminates have higher UBS than blocked laminates, particularly for thicker laminates. They also have higher MCS and SEA for 8 mm and 12 mm pins, but not for 4 mm pins.

It has been reported in [30] that increasing *D/t* ratio leads to lower bearing strength, which agrees with findings here. The authors are not aware of any previously reported correlation between *D/t* and energy absorption. To investigate this, in Fig. 7, the results are plotted as a function of *D/t* (error bars omitted for clarity). Fig. 7(a) shows that for UBS, the dispersed and blocked stacking sequence data separate into two well-defined groups, apart from the outlier mentioned in Main Result 1 above (D4_T1). As shown, both groups can be fitted with a power law equation, with an R^2 value of about 0.75, confirming the observation in [30] that *D/t* ratio is correlated with UBS, for a given stacking sequence. An attempt to fit a single power law equation to *all*

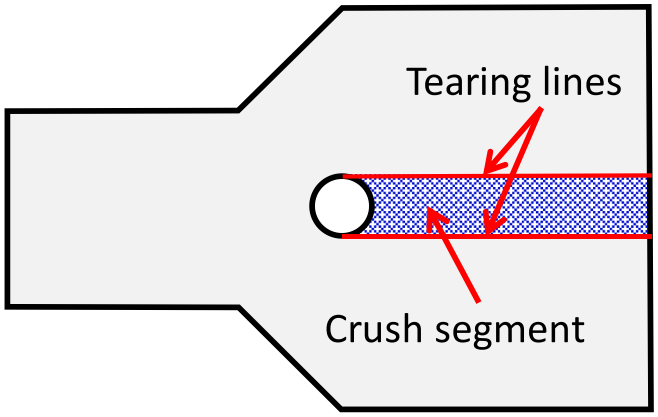

Fig. 8. Crush segment that undergoes crushing and tearing at its edges.

the data however yields an R^2 value of only 0.52, indicating that stacking sequence is an important factor for UBS (see main result 3).

Fig. 7(b) and (c) show MCS and SEA respectively. Remarkably, considering the complex phenomena involved in composite crushing, MCS and SEA show an even stronger correlation with D/t. If the dispersed and blocked stacking sequence data are separated, power law equations can be fitted for MCS with $R^2 = 0.95$ and for SEA with $R^2 = 0.95$–0.97. In fact, a single power law equation can be fitted to *all* the data (including both stacking sequences), with $R^2 = 0.93$ for MCS versus D/t, and $R^2 = 0.95$ for SEA versus D/t, reflecting the fact that the influence of stacking sequence is less well-defined for MCS and SEA than it is for UBS. The fourth main result then is:

Main result 4: D/t ratio is a key parameter in energy absorption of pin-loaded joints undergoing extended bearing failure. Fig. 7(c) can be used to predict the SEA of quasi-isotropic layups of IM7/8552.

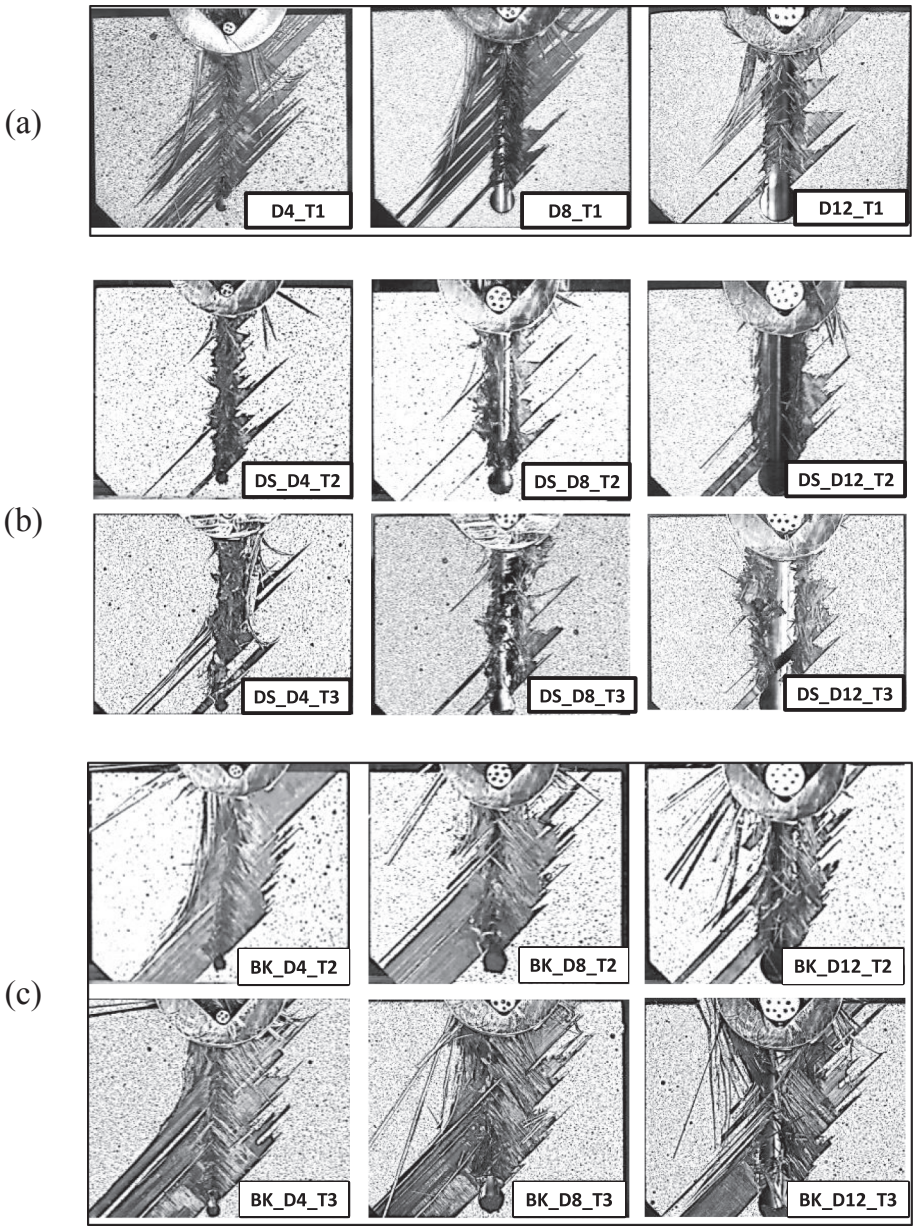

Fig. 9. Final state of one sample from each configuration, (a) 1 mm thick specimens, (b) 2 mm and 3 mm specimens with dispersed stacking sequence, (c) 2 mm and 3 mm specimens with blocked stacking sequence.

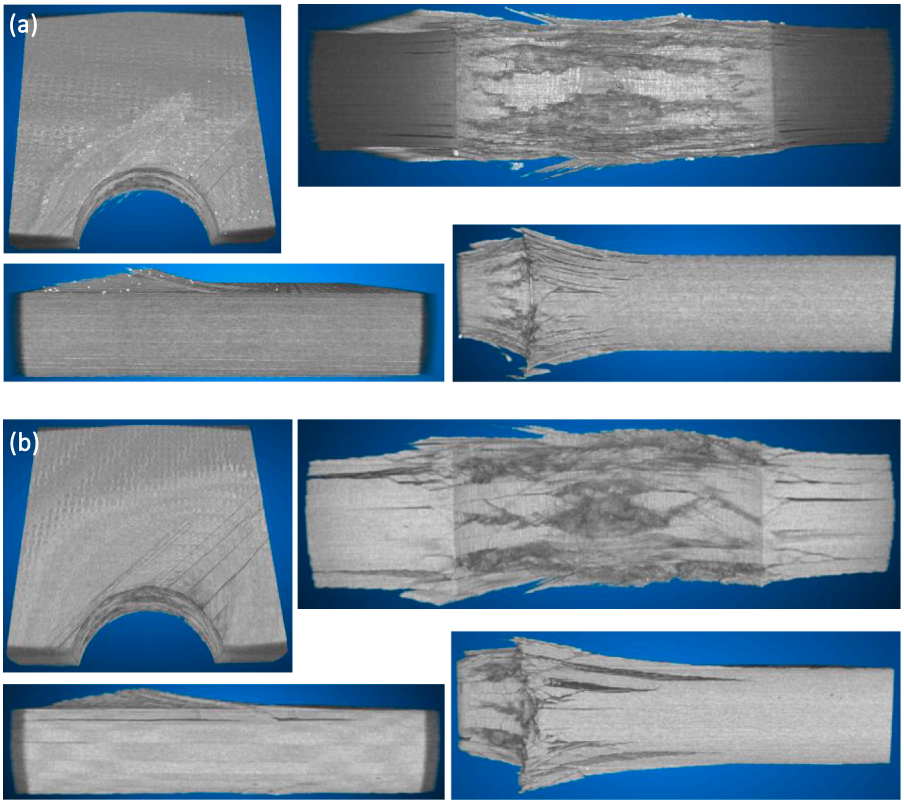

Fig. 10. 3D CT views of (a) DS_D8_T3, (b) BK_D8_T3 specimens (videos showing all angles and slices available in the supplementary information).

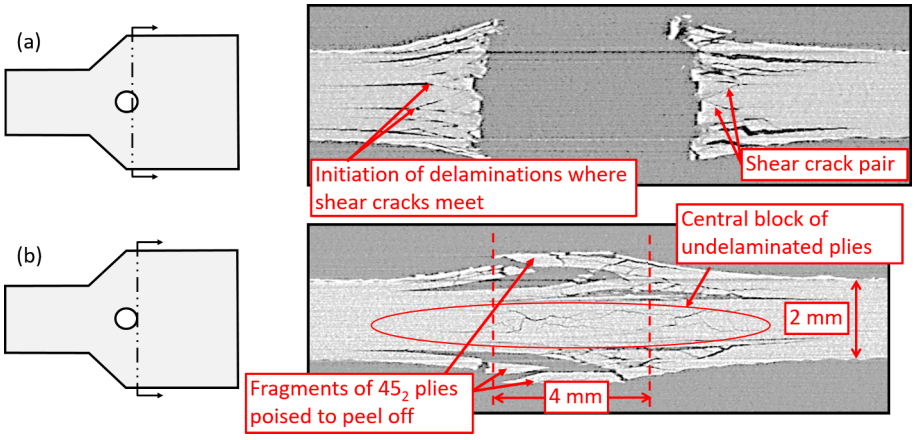

Fig. 11. Transverse sections of interrupted BK_D4_T2 test ($[45_2/-45_2/90_2/0_2]_s$, 4 mm pin).

3.3. Post-test appearance and microscopy

Viewed simplistically, as illustrated in Fig. 8, extended bearing failure involves crushing of a "crush segment" of width D and thickness t, and tearing of the segment from the rest of the laminate. The resistance to tearing changes with thickness but not with pin diameter, while the resistance to crushing varies with both.

However, the real situation is much more complex, as can be seen by viewing the final state of each configuration in Fig. 9. Fig. 9(a) shows the 1 mm thick specimens, Fig. 9(b) shows the dispersed 2 mm and 3 mm thick specimens, and Fig. 9(c) shows the blocked 2 mm and 3 mm specimens. It can be seen that damage extends far beyond the "crush segment" in front of the pin, particularly in the unsupported surface plies. For the blocked specimens, Fig. 9(c), large strips of the outer block of 45° plies have peeled off completely, exposing the –45° ply underneath. For the dispersed specimens, the peeled areas are smaller, and involve only the *one* outer 45° ply. Peeling is more prominent for blocked laminates because the aligned block of outer 45° plies (two in T2 specimens, three in T3 specimens) provide a high resistance to fibre breakage, so delamination presents a lower energy failure path. The energy absorbed by peeling is low, so the process is detrimental to energy absorption. But in a preliminary study, even larger areas of peeling were found when 90° plies were placed on the surface [24]. Placing 0° plies on the surface is not recommended, due to susceptibility to damage, and from an energy absorption point of view the 0° plies are critical, so they should be placed in the interior where they are better supported. A fabric material on the surface may give a better surface-peeling result.

To examine the internal damage state, interrupted tests were performed on 10 of the 15 configurations (boldfaced cases in Table 1), which were then analysed using SEM and 3D CT. The tests were stopped at 0.75 mm of pin displacement which, as can be seen from Fig. 4(b), is

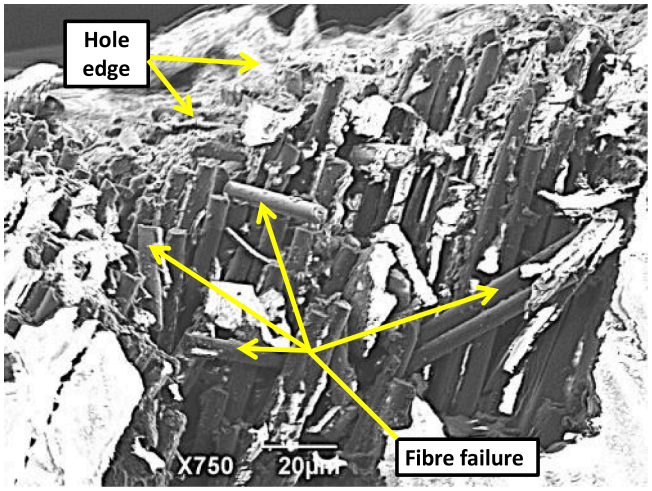

Fig. 12. SEM of interrupted test on DS_D4_T2 specimen ($[45/-45/90/0_2]_s$, 4 mm pin).

just after the occurrence of the peak load. For 3D CT analysis, the specimens were scanned using the XMT instrument Zeiss Xradia 510 Versa (Carl Zeiss X-ray Microscopy, Pleasanton, CA, USA). The field of view was 15 × 15 mm^2 for the D4 and D8 specimens (resolution 15 μm per pixel) and 22 × 22 mm^2 for D12 specimens (22 μm per pixel). Fig. 10(a) and (b) show various views of the DS_D8_T3 and BK_D8_T3 specimens respectively. It is difficult to do justice to 3D datasets in 2D images, so for the benefit of modellers, short videos are included in the Supplementary Information, showing all longitudinal and transverse cross-sections. The CT videos were generated using Dragonfly software, Version 4.1 for Windows.

The dispersed laminate, Fig. 10(a), exhibits more delaminations than the blocked laminate, Fig. 10(b), but the delaminations in the blocked specimen extend further in the loading and width directions. Peeling of the outer three 45° plies of the blocked laminate, as seen above in Fig. 9, is already underway, while only the one outer 45° ply is peeling in the dispersed laminate. Damage is more or less symmetric about the laminate centre, and similar to that of flat plates [31], with outer plies undergoing a relatively low-energy "splaying" mode of failure, and inner plies experiencing a higher-energy "fragmentation" mode.

This is illustrated further in the transverse cross-sections in Fig. 11 of the BK_D4_T2 specimen. Extensive delamination can be seen to the front and side of the hole. As noted by Wang et al. [32], pairs of shear cracks can be seen in Fig. 11(a), aligned about 45° to the loading direction. They result from fibre kinking, fibre-matrix debonding and matrix compression damage. Delamination occurs at locations where two shear cracks meet. From Fig. 11(b) the most severe delaminations occur in the outer plies, while in the centre there is a block of about 8 (of the overall 16) plies which is largely free of delamination. Recalling that the factor of 1.2 in Eq. (3) for SEA is based on an assumption from [16] that the width of destroyed material is 20% larger than the pin diameter, it would seem from the lateral spread of the damage in Fig. 11(b), that the factor may be too low, and a value of about 2 might be better. However, as noted above, 1.2 is retained for comparison with [16]. Values could be scaled by a factor like 1.2/2 if comparison with crushed tubes is desired.

To give a higher resolution view, Fig. 12 shows an SEM image of a dispersed laminate tested with a 4 mm pin. Multiple examples of brittle fibre fracture over short characteristic lengths can be seen. Brittle compressive fibre fracture is the primary contributor to overall energy absorption, due to the high strength of the fibres. The more times each fibre in the 0° plies can be broken along its length (i.e. the shorter the characteristic length of broken fibres), the more energy will be absorbed. Consequently, the lateral support provided to the 0° plies by the other plies is critical. Without lateral support, the 0° plies will bend under the applied pin load and the characteristic length of broken fibres will increase.

Turning to the reasons behind the main results in Section 3.2, Fig. 13 shows longitudinal sections of the loaded side of the hole, for 2 mm thick specimens. The plies are colour-coded to ease interpretation, and blue lines indicate interfaces involving a 90° change in orientation. UBS, MCS and SEA values are indicated, and dashed lines are placed at distances from the hole edge which are multiples of the laminate thickness (2 mm in this case). Dispersed laminates are in the top row, and pin diameter increases from left to right.

For the dispersed laminates, Fig. 13(a), (b), and (c), there are 6 to 9 clearly visible delaminations. Most (but not all) are between interfaces involving a 90° change in orientation, due to the high interlaminar

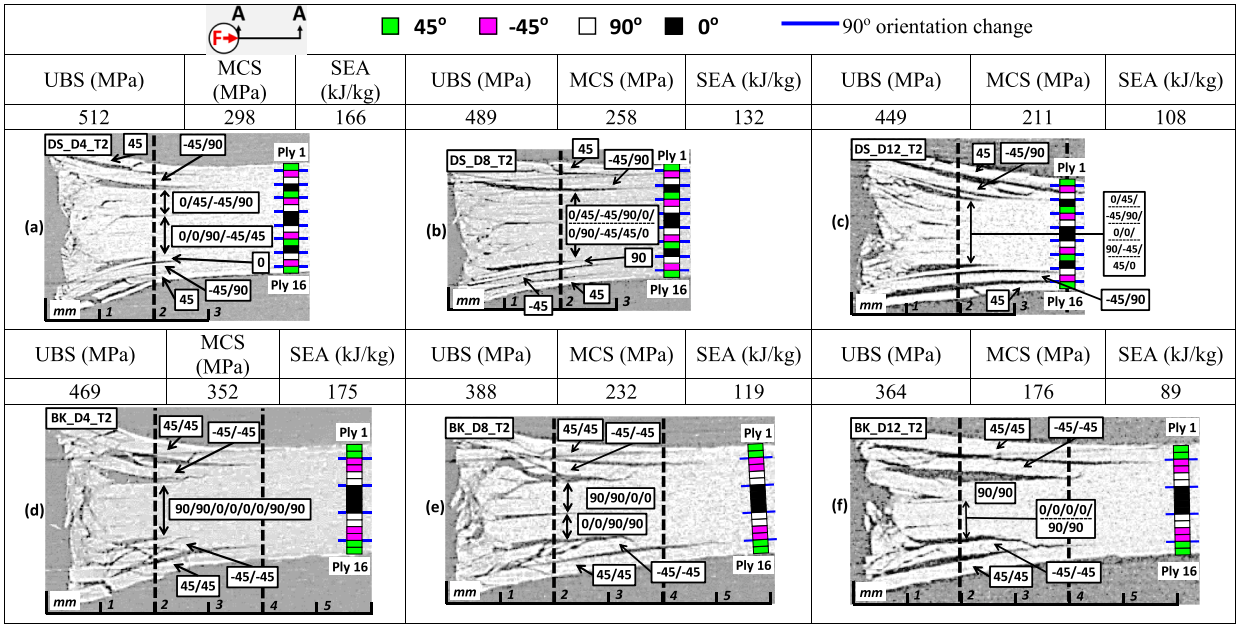

Fig. 13. Effect of pin diameter and stacking sequence on damage in front of hole. Diameter varies across page, top row is dispersed laminate, bottom row in blocked laminate.

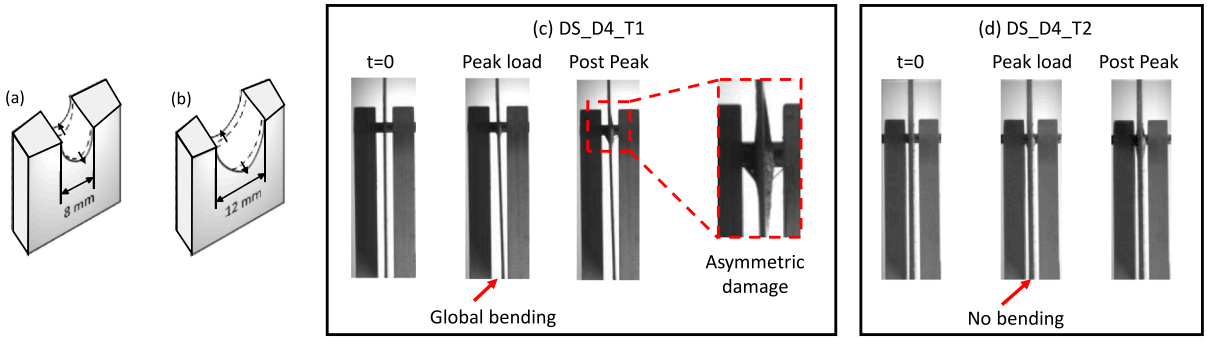

Fig. 14. (a) Brooming deformation at bearing failure with 8 mm pin, (b) 12 mm pin. (c) Global bending of 1 mm thick specimens at peak load and beyond, (d) absence of global bending in 2 mm thick specimens.

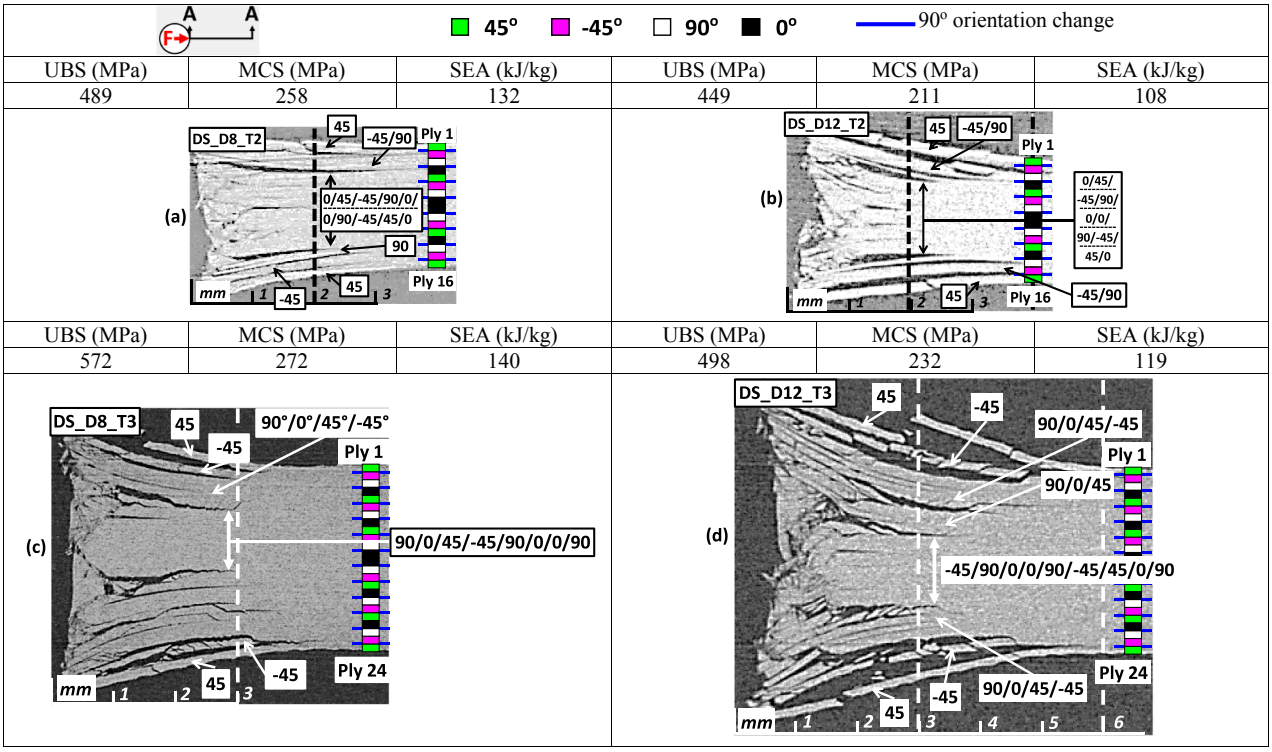

Fig. 15. Effect of laminate thickness on damage in front of hole for dispersed laminates. Diameter varies across page, top row is 2 mm laminate, bottom row is 3 mm laminate.

stresses at such locations. In a few cases, there appears to be a delamination running within a ply (mostly in 0° plies), and delaminations sometimes migrate between interfaces (particularly near the hole edge). Three plies at the top and bottom splay outwards and undergo only small amounts of fragmentation. The inner 9 to 10 plies are heavily fragmented, and thus absorb most of the energy, particularly the four 0° plies in this group. The fragments form debris wedges which force the outer plies outwards.

The key difference between Fig. 13(a), (b), and (c) is the depth of delaminations. As pin diameter increases, the maximum delamination depth increases from about 2.75 mm to over 4 mm. These means that the central plies have less lateral support, so can bend more easily, resulting in lower pin loads. The characteristic broken fibre length is also likely to increase, resulting in less fibre breakages as the pin travels through the laminate. This is one explanation for why MCS and SEA reduce with increasing pin diameter. A second factor is that the force required to tear the material in the crush zone away from the rest of the laminate should not scale with pin diameter (see Fig. 8), so the tearing contribution to MCS and SEA should decrease with pin diameter. As regards why the *UBS* is highest for small pins, Fig. 14(a) and (b) illustrate the "brooming" deformation that occurs at bearing failure, when fibre-kinking occurs, and delaminations initiate. The process is similar to the buckling of a plate, and it can be seen that for smaller diameter pins, the width of the buckling region is smaller, so the buckling load, and hence UBS, is higher. For larger pins, the outer plies have less support against splaying outwards, which is why the delaminations extend deeper into the laminate.

The only exception to the general trends seen for pin diameter is that of the UBS of the 1 mm thick specimens (MCS and SEA of 1 mm specimens followed the general trend). A possible reason is apparent in snapshots from the test videos, shown in Fig. 14(c) and (d). As the load increases to its maximum, the 1 mm specimens undergo global bending, Fig. 14(c), and consequently the damage occurring at bearing failure is less symmetric than for the thicker laminates. In contrast, no bending was seen for 2 mm thick laminates, Fig. 14(d). This bending and asymmetric damage may be the reason why the influence of pin diameter on UBS is slightly different in the 1 mm laminates.

For the blocked laminates, Fig. 13(d), (e), and (f), there are fewer

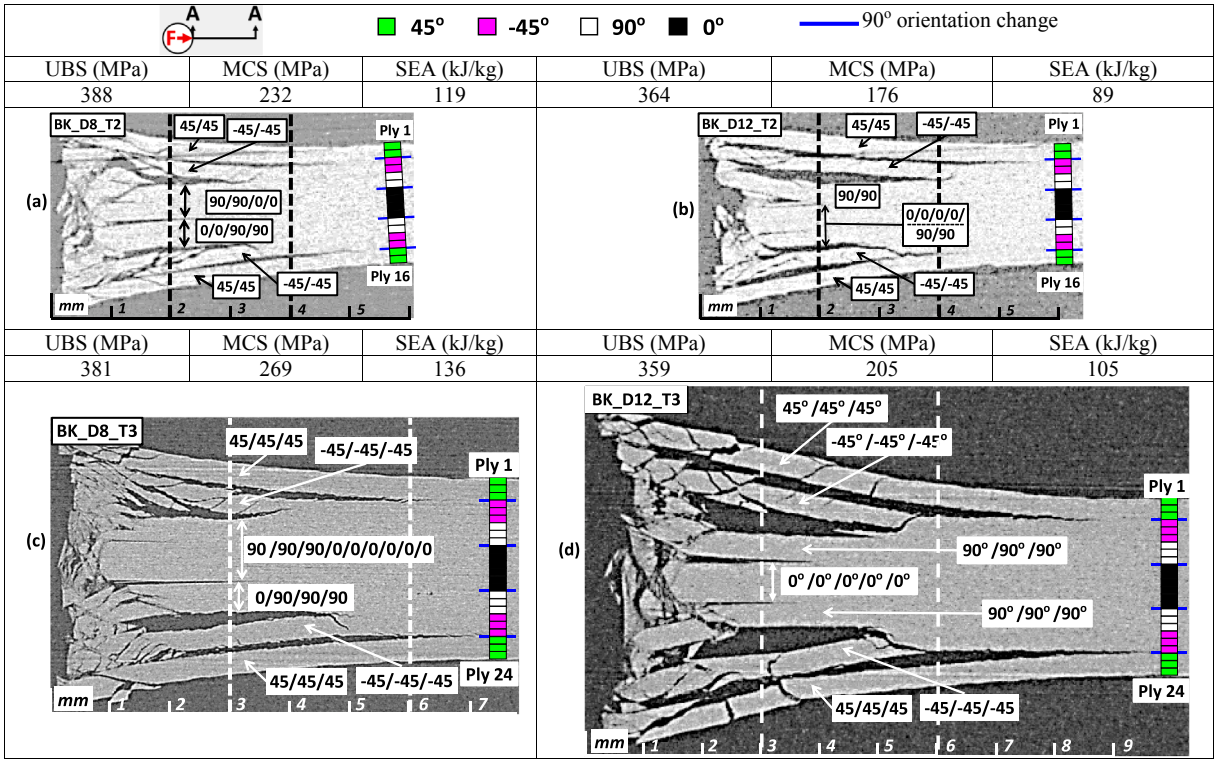

Fig. 16. Effect of laminate thickness on damage in front of hole for blocked laminates. Diameter varies across page, top row is 2 mm laminate, bottom row is 3 mm laminate.

delaminations (4–5), and they occur almost exclusively between the blocks of similarly-oriented plies (apart from one within the central block of four 0° plies). Note that delaminations occur between the blocks of −45° and 90° plies but not so much between the blocks of 90° and 0° plies, even though the latter involves a larger change in ply orientation. Once again, the maximum delamination length increases with pin diameter, this time from about 4 mm to 5.75 mm, and the specific tearing contribution reduces with increasing pin diameter, which explain the reduction in MCS and SEA with increasing pin diameter. The increase in delamination length (1.75 mm) is greater than for dispersed laminates (1.25 mm), which may be why the sensitivity to pin diameter is greater for blocked laminates. The arguments regarding UBS and Fig. 14(a) and (b), equally apply for blocked laminates.

Incidentally, for crushing of flat plates, which could be considered an extrapolation of the current work to an infinite pin diameter, Hobbs and Adams [31] found for HexPly® IM7/8552 (US version: 190 gsm) that delaminations extend far beyond 2*t*, which is in line with the trends observed here.

Concerning the differences between stacking sequences (main result 3), UBS is highest for dispersed laminates at all pin diameters. In the blocked specimens, high interlaminar stresses between ply blocks lead to early delamination and bearing failure. In the dispersed specimens, delaminations need to occur at more interfaces before fibre-kinking and bearing failure can occur. Regarding MCS/SEA, dispersed laminates have the highest MCS/SEA for 8 mm and 12 mm pins, but not for 4 mm pins. The reason could be related to the size and stacking sequence of the central group of undelaminated plies. In each image in Fig. 13, the largest group of undelaminated plies, at a distance of one laminate thickness (2 mm) from the hole edge is indicated. A dashed line is used if a delamination exists within this group which doesn't quite reach 2 mm from the edge. For the 8 mm and 12 mm pins, the dispersed laminates, Fig. 13(b) and (c), have a group of 10 undelaminated plies (albeit with short delaminations within the group), while the largest group of undelaminated plies in the blocked laminates, Fig. 13(e) and (f), is four for the 8 mm pin, and six for the 12 mm pin. The situation is reversed for the 4 mm pin, since the blocked laminate has a group of eight undelaminated plies, while the largest group in the dispersed laminate has only five plies. Delaminations within this critical central group of plies significantly weaken the group's bending stiffness, which would lead to lower pin loads.

The effect of thickness (main result 2), is addressed in Fig. 15 for dispersed laminates, and Fig. 16 for blocked laminates. Comparing Fig. 15(a) and (c) for 8 mm pins, and Fig. 15(b) and (d) for 12 mm pins, it can be seen that the damage does not change in a self-similar manner as the thickness is increased. Increasing the thickness increases the number of potential (and actual) delamination sites. The central group of undelaminated plies, at a distance of one laminate thickness from the hole edge (which is 3 mm for the thicker laminate), is off-centre in the thicker laminate, and the orientations of the plies contained in that group are quite different for the two thicknesses. Thus the crush force does better than simply scale up in proportion to thickness, because there are more delaminations in the thicker laminate. Consequently, UBS, MCS and SEA all increase with thickness.

In contrast, the blocked laminates in Fig. 16 display a greater degree of self-similarity as the thickness increases. The four deep delaminations between the blocks of 45° and −45° plies, and the blocks of −45° and 90° plies remain. These are initiated at the peak load, and resistance to their initiation should not change much with laminate thickness. Thus the peak force scales in proportion to laminate thickness and UBS is unaffected. The reason why MCS and SEA are higher for the thicker laminates may be due to a higher degree of fragmentation in the thicker laminates, which is particularly visible in the outer blocks of 45° and −45° plies. This is likely due to the higher stiffness of a block of three plies relative to a block of two plies, which shifts the failure mode mixity more towards compressive failure and less towards bending failure.

Finally, the large increases in UBS, MCS and SEA as the thickness increases from 1 mm to 2 mm are due to similar reasons, plus the global bucking which occurs in the 1 mm specimens, as seen in Fig. 14(c). Global buckling is likely to have a detrimental effect on the pin load throughout the test.

4. Conclusions

An experimental study has been performed on extended bearing failure of pin-loaded composite joints. Pin diameter and laminate thickness are seen to be important parameters, and can change UBS by a factor of two, and SEA by a factor of nearly three. The D/t ratio proves to be an excellent predictor of UBS, MCS and SEA. For pin diameters between 4 mm and 12 mm, a minimum thickness of 2 mm is recommended to avoid global buckling. Beyond this, increasing thickness will improve UBS but has less effect on MCS or SEA. Small diameter pins should be used. Two small-diameter pins spaced far enough apart (in the width direction) to avoid excessive interference should absorb far more energy than one large diameter pin. Dispersed rather than blocked stacking sequences are found to be marginally preferable for SEA. The extent to which these findings also apply at dynamic loading rates will be examined in future work. The results herein, including the CT scan videos in the Supplementary Information, can be used for validation of models on an extremely challenging problem.

CRediT authorship contribution statement

Jazib Hassan: Conceptualization, Methodology, Investigation, Validation, Writing - original draft, Data curation, Visualization, Formal analysis. **Thomas Feser:** Conceptualization, Methodology, Investigation, Writing - review & editing, Data curation. **Ronan M. O'Higgins:** Conceptualization, Methodology, Supervision, Writing - review & editing. **Matthias Waimer:** Conceptualization, Methodology, Supervision, Writing - review & editing. **Conor T. McCarthy:** Supervision, Funding acquisition. **Nathalie Toso:** Supervision. **Michael E. Byrne:** Investigation. **Michael A. McCarthy:** Conceptualization, Methodology, Supervision, Funding acquisition, Writing - review & editing, Resources, Visualization, Project administration, Formal analysis, Data curation.

Declaration of Competing Interest

The authors declare that they have no known competing financial interests or personal relationships that could have appeared to influence the work reported in this paper.

Acknowledgements

This work was supported by EU Horizon 2020 Marie Skłodowska-Curie Actions Innovative Training Network-ICONIC [grant agreement number: 721256]. The authors would like to thank Ulster University, Belfast, Northern Ireland for their support in cutting the composite specimens.

Appendix A. Supplementary data

Supplementary data to this article can be found online at https://doi.org/10.1016/j.compstruct.2020.111868. The data consists of videos of 3D CT datasets, showing all major cross-sections.

References

[1] FAA. Special Conditions: Airbus A350-900 Airplane; Crashworthiness, Emergency Landing Conditions. Docket No FAA-2013-0892 Special Conditions No 25-537-SC: US Federal Register; 2014.
[2] FAA. Special Conditions: Boeing Model 787-8 Airplane; Crashworthiness. Docket No NM368 Special Conditions No 25-362-SC: US Federal Register; 2007.
[3] Bolukbasi AO, Baxter TR, Nguyen TA, Rassaian M, Davis KR, Koch W, et al. Energy-absorbing floor structure for fuselage of aircraft e.g. civilian or military aircraft, includes coupling units which fix structural members to fuselage frame, floor beam, and support piece. Boeing Co, US Patent Number 8376275-B2; 2013.
[4] Waimer M, Feser T, Schatrow P, Schueler D. Crash concepts for CFRP transport aircraft – comparison of the traditional bend frame concept versus the developments in a tension absorbers concept. Int J Crashworthiness 2018;23:193–218.
[5] Schatrow P, Waimer M. Investigation of a crash concept for CFRP transport aircraft based on tension absorption. Int J Crashworthiness 2014;19:524–39.
[6] Schatrow P, Waimer M. Crash concept for composite transport aircraft using mainly tensile and compressive absorption mechanisms. CEAS Aeronautical J 2016;7:471–82.
[7] Waimer M, Schatrow P, Feser T, Kraft H, Kohlgrüber D. Development of a tension energy absorber – progressive bearing failure mechanisms of composite bolted joints. 8th triennial international aircraft fire and cabin safety research conference. Atlantic City, NJ, USA. 2016.
[8] Goh YM, Love PED. Adequacy of personal fall arrest energy absorbers in relation to heavy workers. Saf Sci 2010;48:747–54.
[9] Thoppul SD, Finegan J, Gibson RF. Mechanics of mechanically fastened joints in polymer-matrix composite structures – a review. Compos Sci Technol 2009;69:301–29.
[10] Camanho PP, Matthews FL. Stress analysis and strength prediction of mechanically fastened joints in FRP: a review. Compos A-Appl Sci Manuf 1997;28:529–47.
[11] Egan B, McCarthy CT, McCarthy MA, Gray PJ, O'Higgins RM. Static and high-rate loading of single and multi-bolt carbon-epoxy aircraft fuselage joints. Compos A-Appl Sci Manuf 2013;53:97–108.
[12] Pein M, Krause D, Heimbs S. Innovative energy-absorbing concept for aircraft cabin interior. Workshop on Aircraft System Technologies (AST). Hamburg, Germany. 2007.
[13] Olschinka C, Schumacher A. Dynamic simulation of flight passenger seats. 5th German LS-Dyna Forum. Ulm, Germany. 2006.
[14] Feser T, Waimer M. Numerical simulation of progressive bearing failure of bolted joints in CFRP aircraft structures. First international conference on impact loading of structures and materials. Turin, Italy. 2016.
[15] Bergmann T. Beitrag zur Charakterisierung und Auslegung zugbelasteter Energieabsorberkonzepte mittels experimenteller, analytischer und numerischer Methoden. Kaiserslautern, Germany: TU Kaiserslautern; 2016.
[16] Heimbs S, Bergmann T. Bearing mode absorber – on the energy absorption capability of pulling a bolt through a composite or sandwich plate. Procedia Eng 2014;88:149–56.
[17] Bergmann T, Heimbs S, Tremmel G, Maier M. Investigation of a composite tensile energy absorption element under static and dynamic loading. ECCM16 european conference on composite materials. Seville, Spain. 2014.
[18] Waimer M, Siemann MH, Feser T. Simulation of CFRP components subjected to dynamic crash loads. Int J Impact Eng 2017;101:115–31.
[19] Kaddour AS, Hinton MJ, Smith PA, Li S. The background to the third world-wide failure exercise. J Compos Mater 2013;47:2417–26.
[20] Koerber H, Camanho PP. High strain rate characterisation of unidirectional carbon-epoxy IM7-8552 in longitudinal compression. Compos A-Appl Sci Manuf 2011;42:462–70.
[21] Kuhn P, Catalanotti G, Xavier J, Camanho PP, Koerber H. Fracture toughness and crack resistance curves for fiber compressive failure mode in polymer composites under high rate loading. Compos Struct 2017;182:164–75.
[22] Koerber H, Xavier J, Camanho PP. High strain rate characterisation of unidirectional carbon-epoxy IM7-8552 in transverse compression and in-plane shear using digital image correlation. Mech Mater 2010;42:1004–19.
[23] Cui H, Thomson D, Pellegrino A, Wiegand J, Petrinic N. Effect of strain rate and fibre rotation on the in-plane shear response of ± 45° laminates in tension and compression tests. Compos Sci Technol 2016;135:106–15.
[24] Hassan J, O'Higgins RM, Feser T, McCarthy CT, Waimer M, Toso N, et al. Investigation of geometrical and composite material parameters for tension-absorbing bolted joints. Twenty-second international conference on composite materials (ICCM22). Melbourne, Australia. 2019.
[25] Wisnom MR. The role of delamination in failure of fibre-reinforced composites. Philos Trans Royal Soc A 2012;370:1850–70.
[26] Li XQ, Hallett SR, Wisnom MR, Zobeiry N, Vaziri R, Poursartip A. Experimental study of damage propagation in over-height compact tension tests. Compos A-Appl Sci Manuf 2009;40:1891–9.
[27] Portemont G, Berthe J, Deudon A, Irisarri FX. Static and dynamic bearing failure of carbon/epoxy composite joints. Compos Struct 2018;204:131–41.
[28] ASTM D5961/D5961M-17, Standard test method for bearing response of polymer matrix composite laminates. ASTM International, West Conshohocken, PA, 2017.
[29] Camanho PP, Lambert M. A design methodology for mechanically fastened joints in laminated composite materials. Compos Sci Technol 2006;66:3004–20.
[30] Collings TA. On the bearing strengths of CFRP laminates. Composites 1982;13:241–52.
[31] Hobbs JM, Adams DO. Laminate design for crashworthiness of carbon/epoxy composites. Aerospace structural impact dynamics international conference (ASIDIC 2015). Seville, Spain. 2015.
[32] Wang H-S, Hung C-L, Chang F-K. Bearing failure of bolted composite joints. Part I: experimental characterization. J Compos Mater 1996;30:1284–313.